remote sensing

MDPI

Article

Investigation of Bored Piles Under Deep and Extensive Plinth Foundations: Method of Prospecting and Mapping with Pulse Georadar

Donato D'Antonio

Independent Researcher, Vicolo III San Nicola n.2, 86013 Gambatesa, Italy; info@tellurad.it; Tel.: +39-3791128093

Highlights

What are the main findings?

- Transillumination velocity tests on the massive plinth provided permittivity values between 5.9 and 6.7; CMP velocity tests on natural soil provided permittivity values between 9.4 and 13.9.
- Backscattering field analysis highlights pile anomalies even in individual radargrams; acquisitions on exposed faces of the excavation reveal unmistakable pile anomalies, in slices, when combined in the form of perimeter tomography.

What is the implication of the main finding?

- It is possible to study piles beneath massive foundations using the transillumination ground-penetrating radar technique. The results indicating the precise position and geometry of the piles are dependent on the availability of trench excavation to below the top of the plinth.
- A simulated prospection of piles under massive plinths, if conducted from ground level, returns results that are very difficult to decode if one does not possess adequate a priori knowledge.

Abstract

Ground-penetrating radar surveys on structures have a wide range of applications, and they are very useful in solving engineering problems: from detecting reinforcement, studying concrete characteristics, unfilled joints, analyzing brick elements, detecting water content in building bodies, and evaluating structural deformation. They generally pursued small investigation areas with measurements made in direct contact with target structures and for small depths. Detecting deep piles presents specific challenges, and surveys conducted from the ground level may be unsuccessful. To reach great depths, medium-low frequencies must be used, but this choice results in lower resolution. Furthermore, the pile signals may be masked when they are located beneath massive reinforced foundations, which act as an electromagnetic shield. Finally, GPR equipment looks for differences in the dielectric of the material, and the signals recorded by the GPR will be very weak when the differences in the physical properties of the investigated media are modest. From these weak signals, it is difficult to identify information on the differences in the subsurface media. In this paper, we are illustrating an exploration on plinth foundations, supported by drilled piles, submerged in soil, extensive, deep and uninformed. Pulse GPR prospecting was performed in common-offset and single-fold, bistatic configuration, exploiting the exposed faces of an excavation around the foundation. In addition, three velocity tests were conducted, including two in common mid-point and one in zero-offset transillumination, in order to explore the range of variation in relative dielectric permittivity in the investigated media.

check for updates

Academic Editors: Xuan Feng, Haoqiu Zhou, Zejun Dong and Roberto Orosei

Received: 5 June 2025
Revised: 9 September 2025
Accepted: 11 September 2025
Published: 18 September 2025

Citation: D'Antonio, D. Investigation of Bored Piles Under Deep and Extensive Plinth Foundations: Method of Prospecting and Mapping with Pulse Georadar. *Remote Sens.* **2025**, *17*, 3228. https://doi.org/10.3390/rs17183228

Copyright: © 2025 by the author. Licensee MDPI, Basel, Switzerland. This article is an open access article distributed under the terms and conditions of the Creative Commons Attribution (CC BY) license (https://creativecommons.org/licenses/by/4.0/).

Thanks to the innovative survey on the excavation faces, it is possible to perform profiles perpendicular to the strike direction of the interface. The electromagnetic backscattering analysis approach allowed us to extract the weighted average frequency attribute section. In it, anomalies emerge in the presence of drilled piles with four piles with an estimated diameter of 80 cm.

Keywords: ground-penetrating radar; pile; common mid point; transillumination; plynth; backscattering field analisys; weighted average frequency, signal attributes

1. Introduction

The study described herein fits into the broad field of applications of ground-penetrating radar (GPR) and, in particular, that of human-made structures. The recent developments [1] in the methods of acquisition, data processing [2] and presentation of results have strengthened a tougher confidence in the use of this tool [3,4]. GPR has been successfully used to study beams, columns, slabs, bridges, tunnels, reinforcing bars, cracks and cracking in concrete, subsidence, stratigraphy, voids and cavities and foundations [5–7]. We describe a method of geophysical prospecting on bored piles, the verification of their number, and the estimation of their geometry under extended foundations on plinth, on which they are constrained, under abutment foundation. The prospecting was carried out in May 2023 at the Liscione Bridge, built between 1967 and 1974, in the Monte Arcano district, on the SS 647 Biferno valley floor, in the province of Campobasso, Molise. An excavation carried out adjacent to an abutment, functional for the maintenance of the drainage around the foundation, uncovered the plinth and surrounding soil and provided a unique opportunity to access the seabed walls and verify the presence and quantity of piles drilled below the plinth. The work performed is important because it allows us to shed light on relatively recent human-made structures for which design drawings are no longer available. Our work represents a turning point, leaving behind all the problems of interpretative ambiguity through the innovative lateral scanning of the excavation fronts. Indirectly investigating, with geophysical methods, the bored piles below the foundations is difficult from the ground surface, especially if the depth between the head of the piles and the ground level is considerable, as in this case, which is 4 m. Especially if it is not possible to access all sides of the pylon, on the surface, the relationships between the geometric variables (Figure 1) and the displacement of the antennas must be favorable; otherwise, the signals coming from the pylon will not be recorded.

For example, assuming a good contrast in dielectric permittivity, f should be very small compared to D; conversely, if f is large, then F should be very small; similarly, D should be much larger than d; E should be at least twice F; and α (and the form of radiation pattern) for low permittivity soils is high and decreases more and more as the permittivity increases [8]. In the following paragraphs a simulation of a direct investigation on the surface is proposed. Surveys are successful when both the transmitter and receiver antennas are sensitive to the target region. For each antenna, this region is defined by the refraction focusing peak, and it depends on the critical refraction angle of the air–earth interface. An estimate of the optimum antenna separation is given by

$$S = \frac{2d}{\sqrt{\epsilon - 1}} \quad (1)$$

where ϵ is the relative permittivity and d is the approximate depth of the target. It should be noted, however, that depth resolution can be increased by the decreasing of the antenna separation. GPR studies of this kind are very recent [5,9], and the need for extraordinary

maintenance for aging civil works is giving a boost to prospecting and research with GPR aimed at these applications.

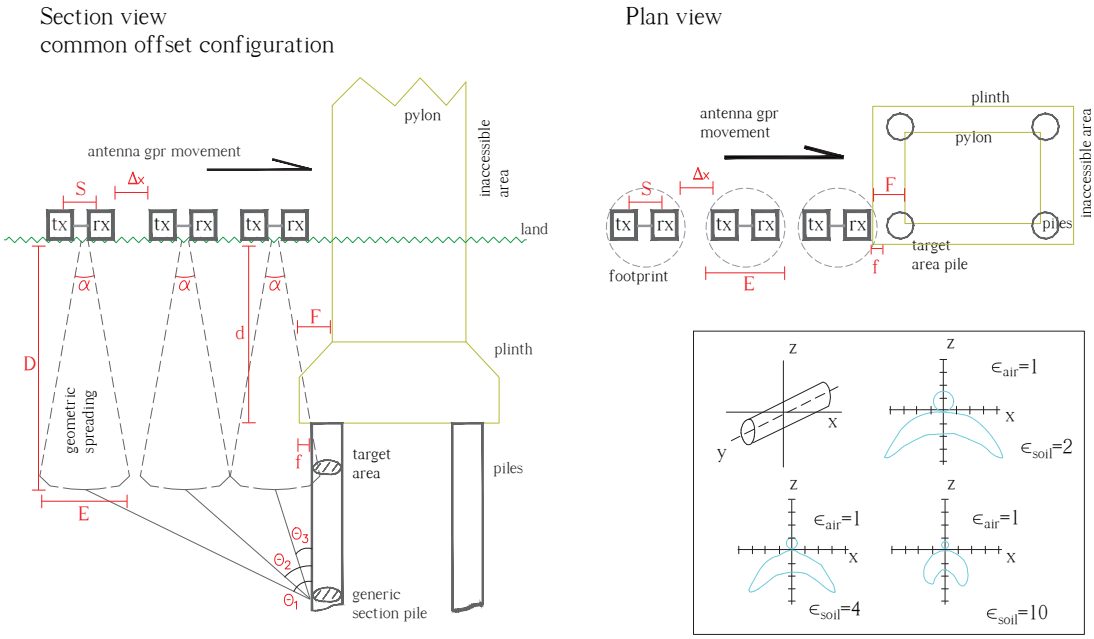


Figure 1. Critical geometric variables, in red, that determine the success rate of a GPR survey of a deep pile beneath a plinth and affect vertical and horizontal resolution; D is the penetration depth, d is the depth of the pile head, E is the energy diameter, α is the opening angle of the illumination cone, θ is the angle of attack between the generic target section of the pile and the base of the footprint, F is the distance of the edge of the plinth from the pile, f is the distance of attachment of the pile measured from the edge of the plinth, Δx is the station spacing that controls aliasing, and S is the antenna separation. The theoretical variation in the radiation pattern [10] with the dielectric permittivity is shown in the box; the cylinder is the antenna orientation.

2. Materials and Methods

Ground-penetrating radar detects dielectric discontinuities and hence makes it possible to investigate objects that are buried in visually opaque media. The dielectric wave has a lot of information that can be related to the parameters significant to hydrology, soil mechanics, and material property characterizations [11]. Moreover, the dielectric wave is also efficient for quantifying the properties of the host materials and the nature and size of the buried superficial bodies as well [12]. The method is based on the transmission of electromagnetic waves through the subsurface to characterize terrains with changes in their electromagnetic properties. The electromagnetic wave propagation is governed by Maxwell's equations [13]. The way that GPR responds to each material is governed by two physical properties of the material: electrical conductivity and dielectric constant. The relative dielectric permittivity (RDP) is a descriptive number that indicates, among other things, how fast radar energy travels through a material. In materials of low magnetic susceptibility, velocity v and attenuation α are related to the RDP ϵ and loss tangent, δ, by the expressions [14]

$$v = \frac{c}{\sqrt{\epsilon}} \tag{2a}$$

$$\alpha = \frac{\omega \cdot \sqrt{k}}{2 \cdot c} \cdot tg\delta \tag{2b}$$

where $\omega = 2\pi f$ is the angular frequency, f is the frequency and c is the velocity of the

EM wave in the empty space (30 cm/ns). There are some main parameters to define for common-offset, single-fold pulse radar reflection survey [15].

Operating frequency: a simple rule of thumb for your choice is

$$log_{10}f = -0.95\, log_{10}z + 6.15 \tag{3}$$

where f is the operating frequency, and z is the required depth of investigation;

time window

$$tw = 1.3\,\frac{2z}{v} \tag{4}$$

sampling interval

$$t = 100\,\frac{6}{f} \tag{5}$$

where t is the time in ns and f is the center frequency in Mhz;

vertical resolution can be taken as one-quarter of the wavelength [16] of the EM wave [17]

$$\lambda = \frac{v}{f} \tag{6}$$

where t is the time in ns and f is the center frequency in Mhz;

horizontal resolution measures for the horizontal resolution of the signal (so-called first Fresnel zone) that can be achieved with a given antenna frequency and in a specified material by

$$r = \sqrt{\frac{\lambda z}{2} + \frac{\lambda^2}{16}} \tag{7}$$

where z is the depth nd λ is the wavelenght;

radius of footprint of the elliptical illumination cone of GPR into the ground is [18]

$$A = \frac{\lambda}{4} + \frac{D}{\sqrt{\epsilon + 1}} \tag{8}$$

where λ is the center frequency wavelength of the EM wave, D is the depth from the ground surface to the reflection surface, and ϵ is the relative dielectric permittivity of the material from the ground to the surface depth (D).

Electrical properties control how electromagnetic waves travel through a material; dielectric permittivity primarily controls wave speed; and conductivity determines the signal attenuation. The relationship between the GPR (transmitter, receiver), buried target distance and the subsurface is described in detail by the radar equation. It is useful both for determining the maximum depth to which the radar can "see" (radar range) and for designing the system itself. Furthermore, it shows that GPR measurements ultimately detect reflected or scattered energy. This ability is governed by the Fresnel coefficient; Fresnel reflection coefficients quantify the amplitude of reflected and transmitted signals at boundaries. The ratio of the reflected-to-incident signal amplitudes is the reflection coefficient; the ratio of the transmitted-to-incident signal amplitudes is the transmission coefficient. Reflection coefficients depend on the angle of incidence, the polarization of the incident field, and the velocity contrast. At the investigated site, the pulsed GPR geophysical prospecting method was used to obtain high-resolution subsurface information. Pulsed GPR surveys use the broadband antennas (UWB) to emit and receive electromagnetic signals from the subsurface. These signals are recorded in the radargrams [13]. The advantages of UWB technology for GPR are as follows:

- It offers high vertical resolution (also known as the down-range resolution), which is closely related to the operating bandwidth [19];

- Covers a frequency range between an octave and a decade by using short-time pulses,

$$\Delta V = \frac{c}{2 \times \Delta f} \tag{9}$$

where Δv is the vertical resolution of the system, c is the velocity of an electromagnetic signal in vacuum, and Δf is the bandwidth used of the system [20].

The radargram is the visual representation of the data recorded by the GPR in a distance-time cross-section. It is composed of a series of successive traces (A-scans), called B-scans. The A-scan is the result of a single radar measurement on an oscilloscope and provides amplitude–time record of a single measurement over a target. At boundaries where the electromagnetic properties of the subsurface change abruptly, radio wave signals can undergo transmission, reflection, and refraction. In this way, the objects present can be studied through signal variations generated by contrasts in their intrinsic physical properties. These variations are defined as signal "anomalies" and they are related to the relative dielectric permittivity (ϵ) and electrical conductivity (σ).

In pulsed GPR, the shape of the transmitted pulse is calibrated to obtain a Gaussian-type spectral distribution [16], where the central value represents the characteristic frequency of the antenna, which corresponds to the dominant frequency of the pulse. It determines the resolution and the maximum exploration depth characteristics. The working hypothesis is based on the question of whether it is possible to reveal the presence of bored piles hidden by a plinth and surrounding soil with GPR. The use of common-offset and single-fold scans on the sides of each exposed face of the foundation could show anomalies if there are contrasts in dielectric permittivity and/or electrical conductivity [14]. To verify this, first we need to explore the site-specific relationship between these variables, depending on the spatial geometry and acquisition method [21]. The sediments encompassing the piles were wet, and we know that the permittivity and conductivity of rocks and soils depend to a large extent on their water content [22]. Both permittivity and conductivity also depend on other properties of the investigated material, in particular on its porosity and clay content, such that the application of such empirical laws should be site- and scale-dependent [23]. The influence of electrical conductivity on the attenuation of the GPR wave can only be neglected in dry soils that do not contain clay particles. In the radargrams, the major signal reflections are related to the dielectric permittivity of the materials involved rather than variations in electrical conductivity [24]. If the contrasts associated with these parameters are weak then the study of the electromagnetic signal and its attributes will be necessary in order to see if the objects can be detected [25]. The attributes from which the best information can be extracted are as follows [26–28]:

- Arc length of time window is defined as the expanded length of the waveform curve within the analysis time window; it is a joint attribute that combines amplitude and frequency characteristics and can be used to distinguish the phase characteristics of GPR records, such as between strong amplitude and high frequency, between strong amplitude and low frequency, between weak amplitude and high frequency and between weak amplitude and low frequency.
- Product of instantaneous amplitude and cosine of instantaneous phase that strengthens the amplitudes of wave peaks and troughs and inverts all trough amplitudes into apparent peak amplitudes.
- Slope of instantaneous frequency is defined as the change rate of instantaneous frequency over time within the analysis time window. It highlights changes in the local frequency, so it can more effectively reflect differences in thin layers, and is effective for dividing edge phases.
- Slope of reflection strength is defined as the change in instantaneous reflection intensity (i.e., instantaneous amplitude) with reflection time. If the reflection intensity remains

throughout the analysis time window interval, the slope value will approach zero. If the reflection intensity gradually increases from the top to the bottom of the time window, the slope value is positive; on the contrary, the slope value is negative. The attribute can reflect the vertical distribution characteristics and interbedding conditions of the stratum.

2.1. Geometry of the Site, B-Scans, and GPR Velocity Tests

In situ, the bridge pylon rests on a trapezoidal plinth. The plinth in turn is constrained to deep bored piles. Geologically, the area consists of upper Pleistocene terraced alluvial soils. The lithologies are mixed-grained: silt, sand, clay and gravel in varying proportions, with the sandy component prevailing; moisture in the exposed soils was evident. From a stratigraphic point of view, the succession of soils on the site is given by the following:

- An 80 cm vegetal cover, starting from the ground level;
- The silty–sandy–clayey soils up to the excavation depth.

The plinth was 10 m long, 8 m wide and 2.3 m high, while the underlying soil was 1.3 m thick to the bottom of the excavation. The base of the plinth was at a depth of about 4 m above the ground level.

2.2. GPR Instrumentation and Acquisition Parameters

The survey was carried out in the spring using a radar system from "Radar System Inc." (Riga, Latvia) with a time range up to 2000 ns, a frequency of pulse repetition of transmitter 115 kHz, 320 scans per second, 1024 samples per scan and stacking of traces up to 128. The antennas used, transmitter and receiver separated, are 200 Mhz, 300 Mhz and 500 Mhz, respectively, and a connecting cable of length 30 m (Figure 2). The antennas are bow-tie, ground-coupled, shielded type. GPR raw data were processed using PRISM 2.54, Georadar-Expert 2.13, Matlab 2020, Seismic Unix 40. This combination of tools enabled sophisticated data analysis and visualization, enhancing the quality of the survey results. Preliminarily, the propagation of the electromagnetic wave was simulated qualitatively in the time domain to understand how different center frequency antennas could perform, as well as to get an idea of how the A-scan might look like in the given conditions [29]. The positioning was achieved with metric measurements of the entire site and plinth geometry in order to obtain a 3D reconstruction (Figure 3). The scans were measured and marked using some spray references.



Figure 2. Excavation of the foundation for drainage maintenance and acquisition steps with the antennas, control unit, and connection cable reel.

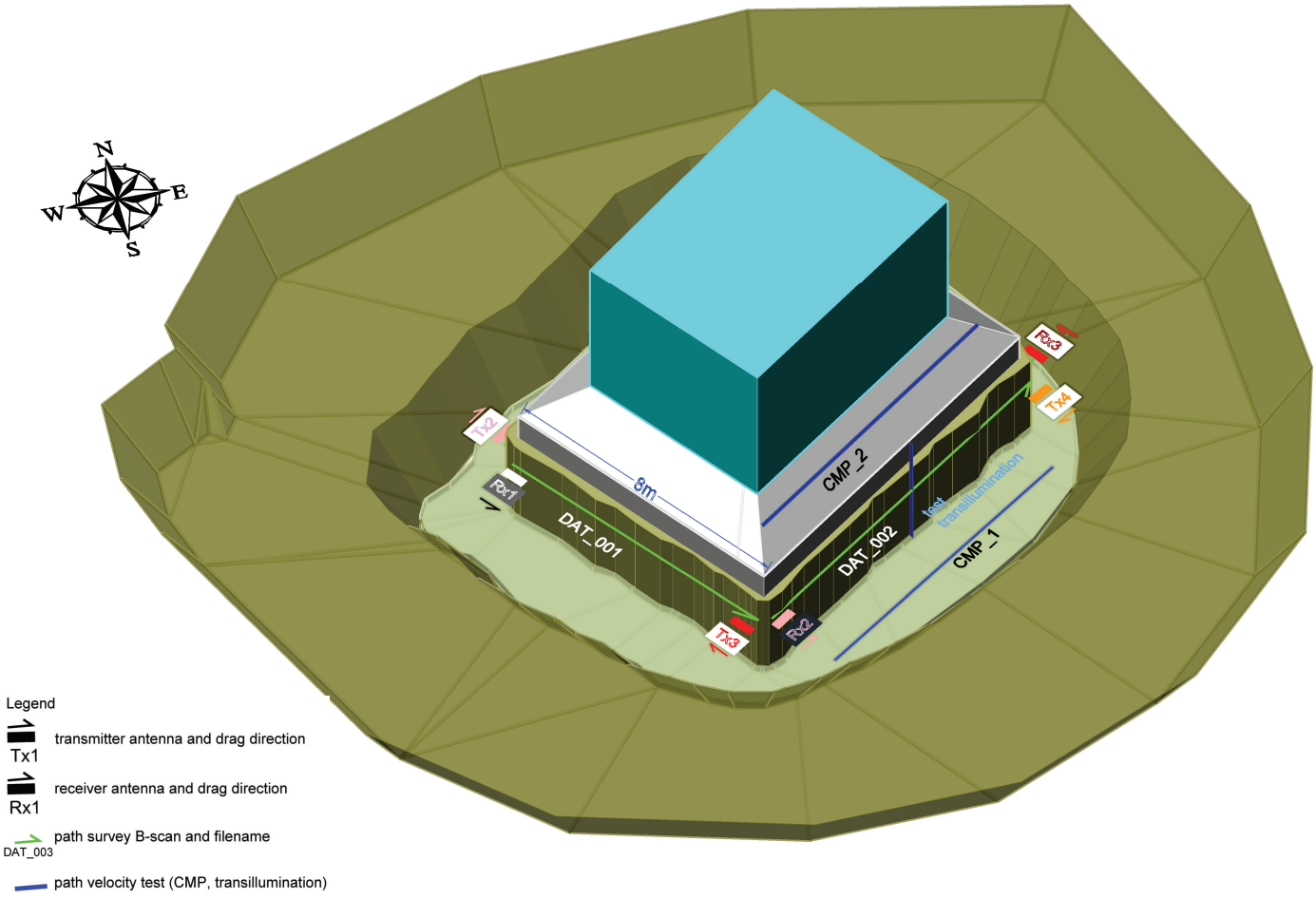


Figure 3. 3D view of the site: The stations of the 2 CMP tests, the transillumination test, and the 4-sided B-scans are shown with the location of the transmitting and receiving antennas, for each acquisition, drag direction and filename.

2.3. Direct In Situ Velocity Tests: CMP and Zero-Offset Transillumination

For the calibration of the propagation speed of the electromagnetic wave in the medium, the following in situ velocity tests had to be carried out:

- One test of the common mid point on the excavated bottom;
- One test of the common mid point on the exposed plinth;
- One test transillumination zero-offset on the two faces of the short side of the foundation.

The two CMPs were performed by symmetrically moving 2 antennas with a constant step, a 500 Mhz transmitter and a 300 Mhz receiver, along the same direction and each in opposite directions starting from a common midpoint (Figure 4). The CMP method is suitable for building structures [30].

In the CMP test the constraint is that the process requires more time to survey a site, since the transmitter and receiver must be moved independently from each other for every scan [30].

To determine the velocity in the crossed medium and so the relative permittivity, the following trigonometric relation can be applied:

$$vt_n = 2\sqrt{(x - x_0)^2 + (\frac{vt_0}{2})^2} \tag{10}$$

where the time of flight of the signal t_n is the time the signal needs from the transmitter and back to the receiver, while t_0 is the time to and from the target at the coordinate of

the minimum distance (x_0). From the survey schematic, we see that if the interface is approximately flat, the point of reflection is the same for all readings. As a result, the signal from the reflected wave in the radargram should form a hyperbola (Figure 5). The advantage of the CMP test is that the receiver does not become saturated while receiving the reflected signal [30]. The radargrams of the CMP acquisitions can be seen in the following figure, wherein the gray box of each are calculated the results of the velocities and permittivities, shown in detail in Table 1. The zero-offset transillumination test between the transmitting and receiving antennas was possible by having 4 vertical faces, with the grounds to be tested, exposed. The antenna used for receiving was the 300 Mhz and transmitting the 200 Mhz. The center-band frequency was 195 Mhz and the wavelength in the medium was 0.4 m, which was optimal to avoid near-field problems since the two opposite faces of the short side stood 8 m apart, which is much more than 1.5 times the wavelength. The 2 antennas were moved from top to bottom with point acquisition every 10 cm.

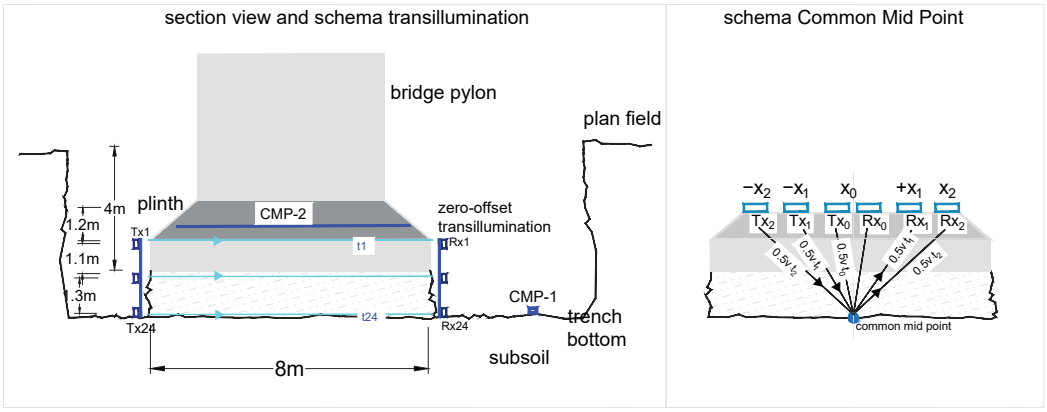


Figure 4. Geometry of the acquisition area, CMP tests, and zero-offset transillumination.

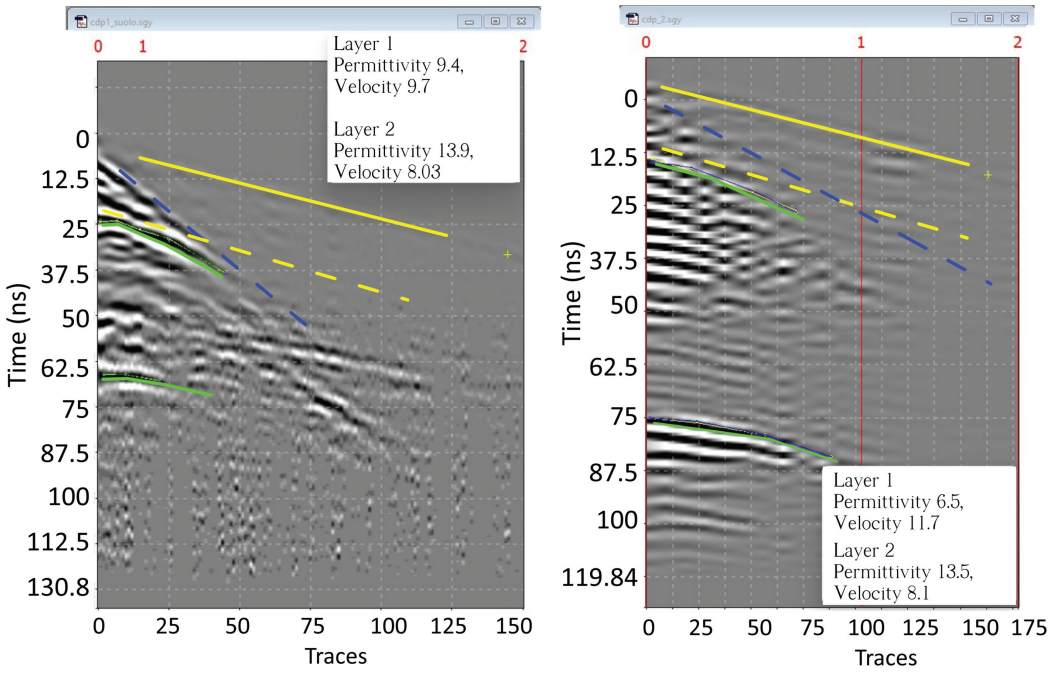


Figure 5. CMP1 radargrams on the left and CMP2 on the right. The free airwave has been highlighted with the solid yellow line, the dashed yellow line instead of the critically refracted airwave, the blue dashed line for the ground wave and the lines in green for the refracted waves.

Table 1. Velocity and dielectric permittivity of the tested layers.

	CMP1 on Trench		CMP2 on Plynth	
	Layer		Layer	
	1	2	1	2
Thickness (m)	0.96	1.68	1.1	2.47
Layer velocity (cm/ns)	9.79	8.04	11.74	8.15
Permittivity	9.4	13.94	6.53	13.56
Error [RMS]	0.11	0.02	0.32	0.001

The distance measured at the top and bottom of the excavation was always 8 m on the short side. A total of 24 "illuminations" were made. The waves received and the traces of each measurement point are shown in Figure 6. To calculate the airwave, the length of the perimeter path on the ground between the two antennas is required. This is 11 m when the antennas are on the top of the plinth and 16 m when the antennas are on the base of the trench. The first arrival in these B-scans can be identified as the first significant change in amplitude. The period of small or no response in each trace is the time elapsed by the pulse between the transmitting and receiving antenna on the other side of the exposed face. In the radargram, through appropriate trace gain, the entire portion from 70 ns onwards takes on much greater prominence than the first part; these signals have higher amplitude than the first arrivals of the wave in the air. This is because for the signal that travels only in air, the transmission and reflection coefficients do not vary since the permittivity is always the same.

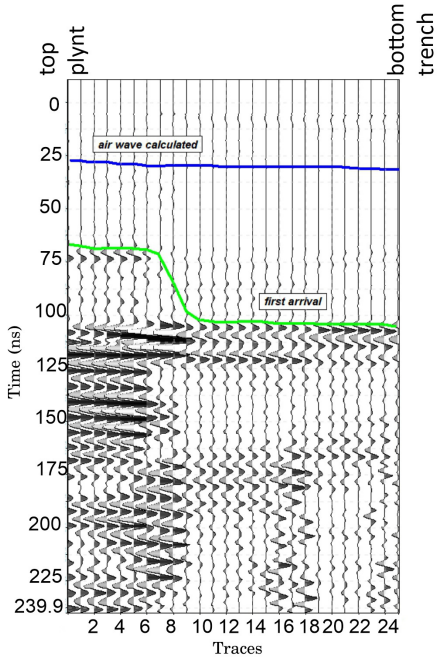


Figure 6. Wave arrivals in the transmission test. In blue are the calculated potential arrivals of the wave in the air, and in green, the first arrivals of the direct wave.

2.4. Acquisition B-Scan GPR

Four B-scan profiles were acquired in single-fold mode. The 200 Mhz transmitting antenna is placed on one side of the trench, at the base of the excavation, while the 300 Mhz receiving antenna is placed on the opposite side and on the same reference line with respect to the cardinal points (Figure 7). The GPR step is 0.01 m and the spatial separations of the transmitting and receiving units are as follows:

- For 200 mhz, $\Delta x = 70$ cm;
- For 300 mhz, $\Delta x = 68$ cm;
- For 500 mhz, $\Delta x = 45$ cm.

The antennas were used to acquire data sequentially, where each one transmits and receives simultaneously, then operating the data fusion.

The antennas used are dipolar and radiate with a preferred polarity (parallel endfire). The antennas are normally oriented so that the electric field is polarized parallel to the long axis or strike direction of the target. The antenna's illumination cone is extended perpendicularly to the exposed face of the trench where the antenna is placed (Figure 8).

In this way, the transmitted electromagnetic energy passes through the adjacent layers it encounters. In this case, all the terrain and objects along the radiation pattern are struck: a first layer of soil, then the concrete plinth, then the soil, then the concrete plinth again, and so on. The antenna orientation dictates the direction of the electric field (E) in the subsurface. *E-field* direction, in turn, dictates how well a target will couple to the excitation field and generate a measured reflected or scattered signal. Antennas are copolar and normally oriented to the target, which is not equidimensional.

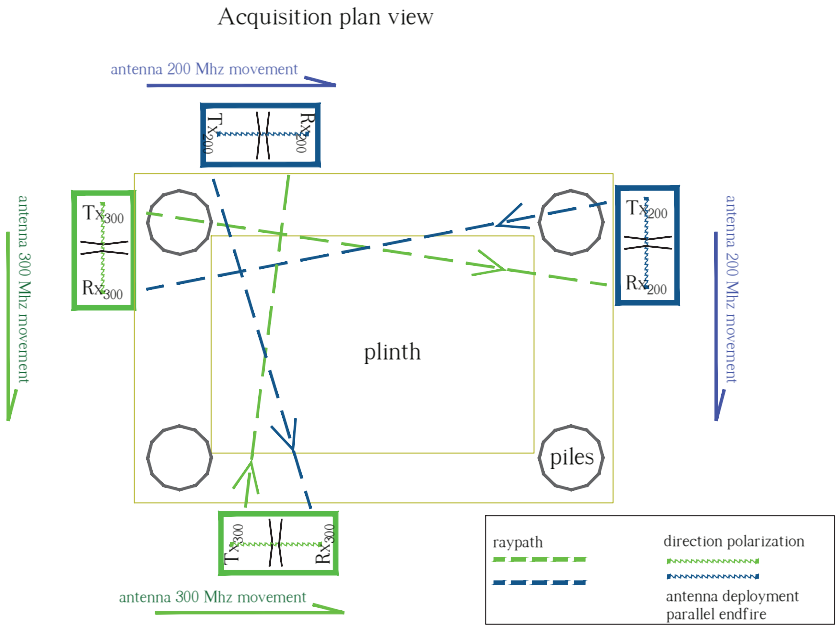


Figure 7. Plane view acquisition geometry of the B-scans on the exposed faces of the trench: relationship between the antenna deployment, polarization direction, raypath, and target. The arrow indicates the direction of the transmitting signal. The electric field is assumed to be aligned along the antenna's long axis.

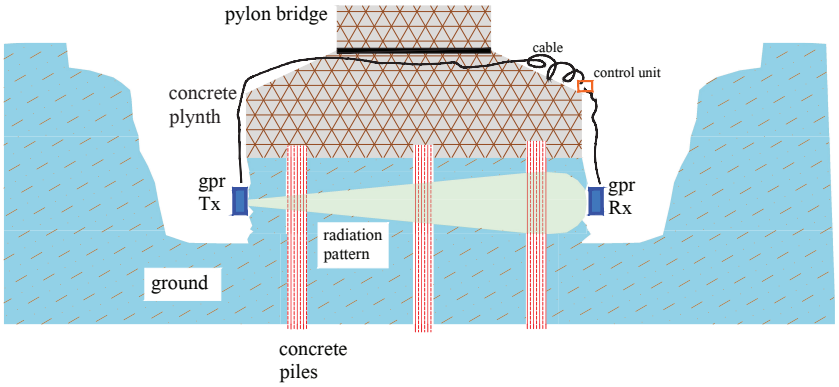


Figure 8. Schematic of B-scan acquisitions with separate Tx and Rx antennas placed on opposite sides of each side of the bottom trench, the long cable connecting to the control unit.

The acquisition parameters are grouped in Table 2 in the first 4 columns; in the remaining ones are the values estimated using $f = 300$ Mhz, $\epsilon_{mean} = 12$, and $\sigma_{mean} = 0.5$ mS/m.

Table 2. Acquisition parameters in bistatic configuration.

Time Window (ns)	Stack Traces	Sample	Realtime Filter	Wavelength Medium (m)
200	4	512	no	0.27
1/2λ; 1/4λ	**Fresnel zone foot (m)**	**$f_{Nyquist}$ Mhz**	**Loss tangent**	**Q-estimation**
0.14; 0.07	2.2; 1.1 [1]	1280	2.24	30

[1] First, number is semimajor axes and second is semiminor axis.

The acquired radargrams are, here, grouped in the form of horizontally compressed wiggle plots (Figure 9). The wiggle plot is a collection of single traces with no color intensity, and the visual aspect focuses on the shape and pattern of the data, on the deviation in positive and negative values from a baseline such as the reference polarity. The polarities, positive and negative, of the reflection provide much information about the type of material from which it comes. A change in polarity can help in the interpretation of data by indicating a transition from a metallic to a plastic object, for example.

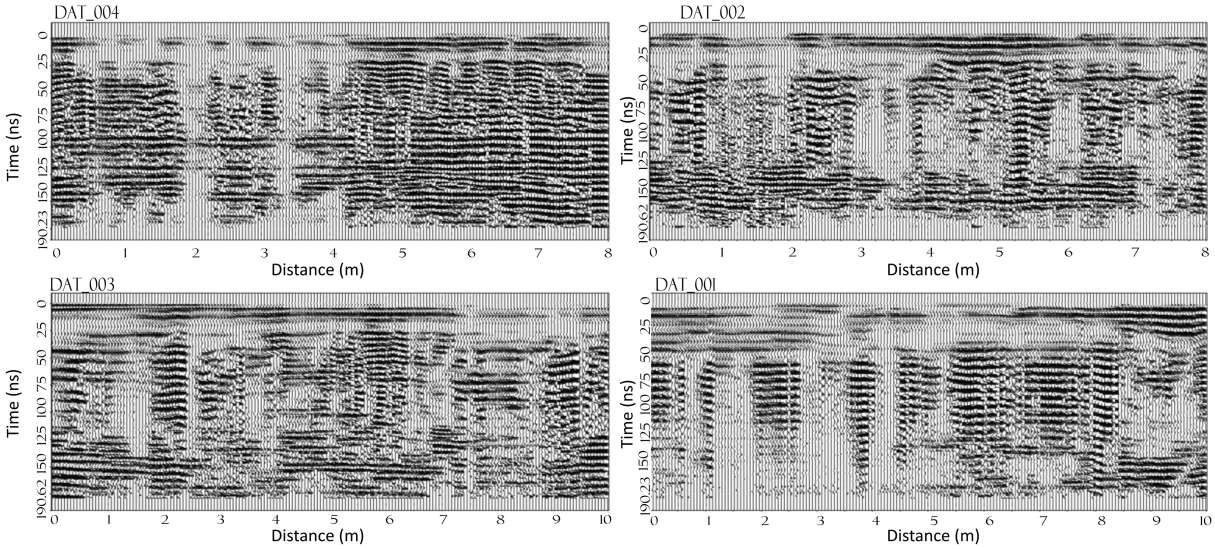


Figure 9. Radargrams from DAT_001, bottom right, to DAT_004, top left. The wiggle plot shows the combination of a series of A-scan.

2.5. Processing GPR Data

In order to generate GPR signals with adequate signal-to-noise ratio (SNR) and to extract meaningful information from the radargram, GPR data processing is implemented. The following data processing helps to reduce clutter or eliminate unwanted noise in the data set:

- Time-zero correction to ensure that all reflections are correctly aligned by setting the airwave and direct wave of the trace at the first break point (or the first negative lobe) to a particular time-zero position.
- Background signal removal that is present at the beginning of a radar signal known as the direct wave, which is due to the coupling of the antenna with the vertical face of the trench. This part of the signal is considered as unwanted noise or clutter.

- Exponential gain to equalize the amplitude of the emitted wave, which suffers a significant attenuation along the medium.
- Ormsby bandpass filter along a trace for low-frequency interference and signal's high-frequency components suppression. The algorithm used comprises three steps: application of direct FFT (fast Fourier transform) for transition from the time domain into the frequency domain of low-frequency and high-frequency trace spectrum components suppression and application of reverse FFT for transition from the frequency domain into the time domain; the cutoff frequencies are from 30 to 110 Mhz (in low frequency) and 230 to 340 Mhz in high frequency.
- Time-depth conversion should be used for restructuring the initial time profile into a depth profile in compliance with the velocity areas.

2.6. Backscattering Electromagnetic Field (BSEF) Analysis

There are situations, even very common ones, in which the geophysical characteristics of the subsurface change fluidly, without jumps. This is due to the diffuse nature of the adjacent layers. In these situations, it is difficult to distinguish the variations or the reflections [31] from the GPR signal recordings with visual analysis of the radargrams. The only solution is to manually determine, as is well known in geophysical techniques, the velocity characteristics of the various discontinuities in the radargrams based on the diffracted waves and combine the areas with similar velocity values into layers. The diffracted waves are formed following reflections from point-like objects in the subsurface based on their cross-sections affected by the energy. The cross-section is a measure of the effective area that a scatterer objects into the path of the incident radar signal. The incident radar wavefront energy per unit area multiplied by the cross-sectional area determines the energy the scatterer extracts from the incident wave.

The energy-extracted signal can be absorbed or re-radiated in any direction. Scattering describes deviations in the paths of electromagnetic waves due to localized non-uniformities, which are less than 1/4 the wavelength of the radio wave signal; backscatter gain measures the amount of energy re-radiated back in the direction of the incident signal. Backscatter gain and cross-sectional area are either computed from numerical modeling or measured for standard geometrical shapes in laboratories. Some simple geometries yield relatively compact analytical backscatter gain formulas. The cross-sectional area is a function of the true geometrical cross-section of an object as well as the contrast in electrical properties. The backscattered gain is primarily controlled by the geometrical attributes of the object. When an electromagnetic wave impinges on the interface between two media with different dielectric properties, a part of its energy is backscattered [32,33] and the remainder is transmitted into the lower medium.

The directions of the incident, reflected and transmitted waves are related to each other by Snell's law. The radiation pattern in the real case of inhomogeneous media becomes increasingly diffuse, and backscattering tends to increase. Part of the transmitted energy is scattered at the inhomogeneities and can pass through the upper medium to the surface [31]. Scattering, which is called volume scattering, is weaker than surface scattering because it causes a redistribution of energy in the transmitted wave in multiple directions, resulting in energy loss. The total loss that an electromagnetic wave experiences in a physical medium is the sum of the loss due to diffusion and the loss due to conduction [34]. The radar backscatter of an object, as mentioned by Toropainen [35], is measured in decibels (dB) using Equation (11) (the equation is used in the routine for automatic calculation of BSEF analysis sections):

$$\sigma_{cp} = \sigma_s \perp [\frac{1 - e^{-2\sigma_t d}}{2\sigma_t} + 2[\Gamma_2]^2 d e^{-2\sigma_t d} + \frac{|\Gamma_2|^4}{2\sigma_t} e^{-2\sigma_t d}(1 - e^{-2\sigma_t d})] \quad (11)$$

where the first term represents the backscatter of the incident wave; the second term represents the forward scattered wave; the third term represents the reduced incident wave's backscatter; Γ_2 represents the voltage reflectance coefficient at the lower surface; σ_t represents the cross-section of the material; σ_s represents the co-polarized cross-section of the material, and their angular variation is according to Fresnel reflectivity of two types of polarizations; and d is the distance traveled by the signal. With these reflection patterns, recorded in the radargrams, the properties of the investigated materials can be extracted directly through dedicated processing.

From this premise, it seems natural to use the backscatter field [36] of electromagnetic waves to determine the physical structure (electric and magnetic) of the propagating medium [37]. One of the advantages of BSEF analysis is the ability to study the subsurface, whose physical (electric and magnetic) characteristics change vertically and uniformly, without sudden jumps, and they cannot form reflections. In such soils, often, only high-frequency noise and various types of interference are present on the GPR profile, provided that the medium does not contain local objects. Local subsurface objects are defined as those whose linear dimensions are comparable to the wavelength of the GPR antenna pulse and whose physical characteristics differ from those of their encompassing medium [33]. They become a source of diffracted waves, whose kinematic and dynamic characteristics contain information about the properties of the subsurface. With this analysis, the attribute sections are obtained [36] to study the subsurface even in the absence of reflections from the layer boundaries. The backscattered wavefield attributes of the GPR profile are quantitative characteristics of a recording. Based on the wavefield attributes, subsurface parameters such as permittivity, humidity, electrical resistivity, conductivity, amplitude, frequency, phase, attenuation, etc., are calculated. In our processing, the attribute section Weighted average frequency was studied, which is the weighted average frequency [33] of the spectrum of the reflected signal, calculated by the formula,

$$F_{wa} = \frac{\sum A_j F_j}{\sum A_j} \tag{12}$$

where A_j is the spectral amplitude at the frequency F_j measured in MHz.

3. Results

Survey results are represented in the following order: velocity tests, bistatic scans, and common-offset single-fold measurements.

Velocity Test Results

The results of the two CMP velocity tests, shown in Table 3, demonstrate that the velocity of the EM wave undergoes a clear variation propagating through the plinth and then into the encompassing soil. The velocity of the soil outside the plinth also shows values consistent with the lithologies present. In addition, the clay component of the soils and their moisture did not result in a lowering in propagation velocity. In the transillumination test, first arrivals, distances and depths of travel of antennas were measured (Table 3). Knowing the horizontal separation between antennas and the travel time of the radar energy at each point, the velocity and relative dielectric permittivity can be calculated. The velocity measurements, at each point, thus represented as a function of antenna depth, show the trend in the tested material, any gradient or whether there are jumps (Figure 10). In this case, a dip between 70 cm and 100 cm depth is noted (measurements started from above), which corresponds to the interface between the plinth and the underlying soil on which it rests. The conducted velocity tests were used to explore the dielectric permittivity field across the media to be investigated and used them for BSEF analysis.

Table 3. Zero-offset transillumination test results.

Trace	Depth (cm)	Distance (cm)	Time (ns)	Velocity (cm/ns)	ϵ
1	0	800	65.27	12.26	5.98
2	10	800	66.86	11.97	6.28
3	20	800	67.44	11.86	6.39
4	30	800	66.86	11.97	6.28
5	40	800	66.86	11.97	6.28
6	50	800	66.86	11.97	6.28
7	60	800	67.44	11.86	6.39
8	70	800	69.2	11.56	6.73
9	80	800	85.04	9.41	10.15
10	90	800	96.18	8.32	12.99
11	100	800	97.94	8.17	13.47
12	110	800	97.94	8.17	13.47
13	120	800	98.52	8.12	13.63
14	130	800	99.11	8.07	13.79
15	140	800	99.7	8.02	13.96
16	150	800	100.87	7.93	14.29
17	160	800	105.87	7.56	15.74
18	170	800	104.46	7.66	15.32
19	180	800	105.35	7.59	15.59
20	190	800	104.9	7.63	15.45
21	200	800	105.66	7.57	15.68
22	210	800	105.75	7.56	15.71
23	220	800	106.57	7.51	15.95
24	230	800	106.92	7.48	16.05

During the GPR investigation of the soil under the foundation, four GPR profiles were recorded. Analysis of each of these B-scan GPR profiles produced no results and no visual evidence of amplitude anomalies that could be directly interpreted from radargrams and correlated with the target under investigation (Figures 11 and 12). In the two radargrams reproduced here (Figures 11 and 12), the areas (red boxes) with some of the most evident reflections have been highlighted, which are distributed along the entire length.

The average spectrum is very narrow, and the peaks with the highest spectral density are at 141 Mhz and 134 Mhz. The attenuation curves fluctuate within about ten decibels from zero. We would expect to find sharp, narrow, well-defined signal discontinuities at the beginning and end, or hyperbolas for the piles, but there is no evidence of it. It became necessary to combine these 4 profiles into a single set.

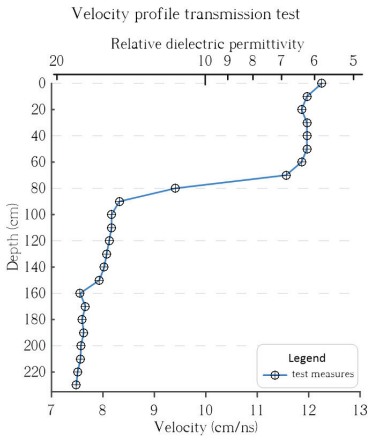


Figure 10. Graph of velocity and dielectric permittivity ϵ (in logarithmic scale) as a function of measurement depth.

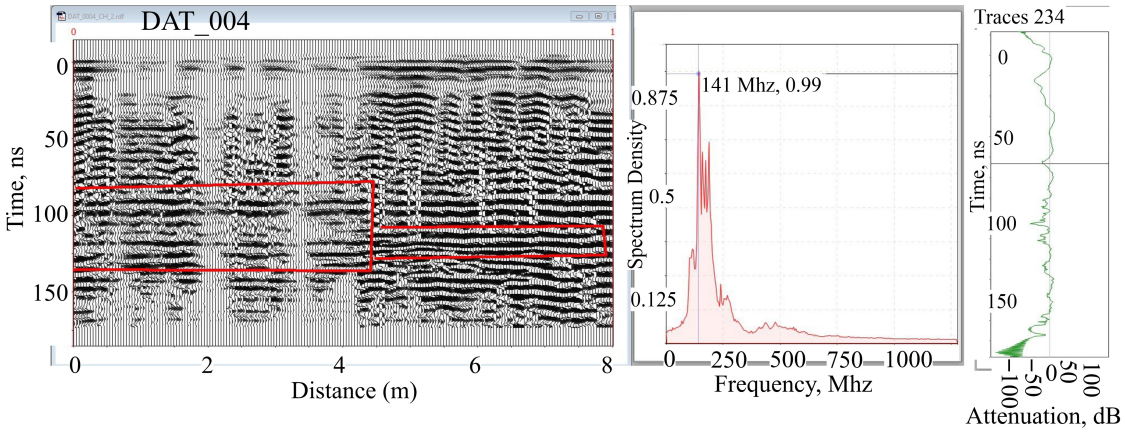


Figure 11. Processed radargram DAT_004, with relative attenuation curve of trace 234 and spectrum, where the spectral density peak at 141 MHz is highlighted.

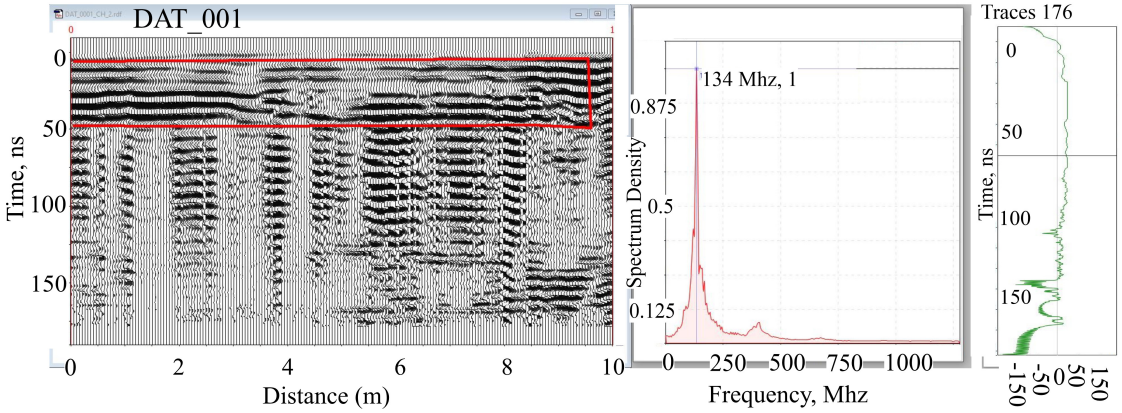


Figure 12. Processed radargram DAT_001, with relative attenuation curve of trace 176 and spectrum, where the spectral density peak at 134 MHz is highlighted.

In general, this can be achieved easily if the GPR profiles have the pulses propagating in one direction. In this particular case, however, the antenna radiation propagates in the same plane but in different directions as the antennas move along a perimeter. With the help of BSEF analysis, the sections of the four radargrams of the attribute "Weighted Average Frequency" were first combined to obtain a perimeter tomography. In GPR data processing, A-scan traces are sequentially plotted as B-scan profiles. Often, direct interpretation of each individual profile may be sufficient when the geology or stratigraphy of the subsurface is not complex. In complex cases, analysis of the spatial distribution of the amplitudes of the reflected waves is used, as shown on the left of Figure 13.

However, compared to the Cartesian plane, in this left section of the figure we have many radargrams (B-scans 1 to *n*) where the propagation direction of the electromagnetic signal is always the same. In our case, shown on the right, we have four radargrams whose signal propagates on the same plane in different directions. To combine these signals, it was first necessary to separate the radargrams into pairs with similar propagation directions but with opposite directions. For example, B-scans d1 and d3 are grouped into a first group, and B-scans d2 and d4 are grouped into a second group.

The next step consists of inverting the traces of one of the two radargrams along the t-axis of the B-scan so that the traces of the two radargrams in a group have the time direction pointing in the same direction. This inversion can also concern the x-axis if, for example, d1 was acquired towards the east and d3 towards the west. In fact, the opposite radargrams (d1–d3 or d2–d4), when taken in pairs, cover a positive half-space and a negative half-space with respect to the distance-time axes. Subsequently, the processing is analogous to the

extraction of amplitude-averaged time slices from co-polar radargrams, where the same area is illuminated first by a signal polarized in one direction and then by a signal polarized in another direction perpendicular to it. In Figure 14, we can appreciate the results of the BSEF analysis of individual radargrams using the weighted average frequency attribute.

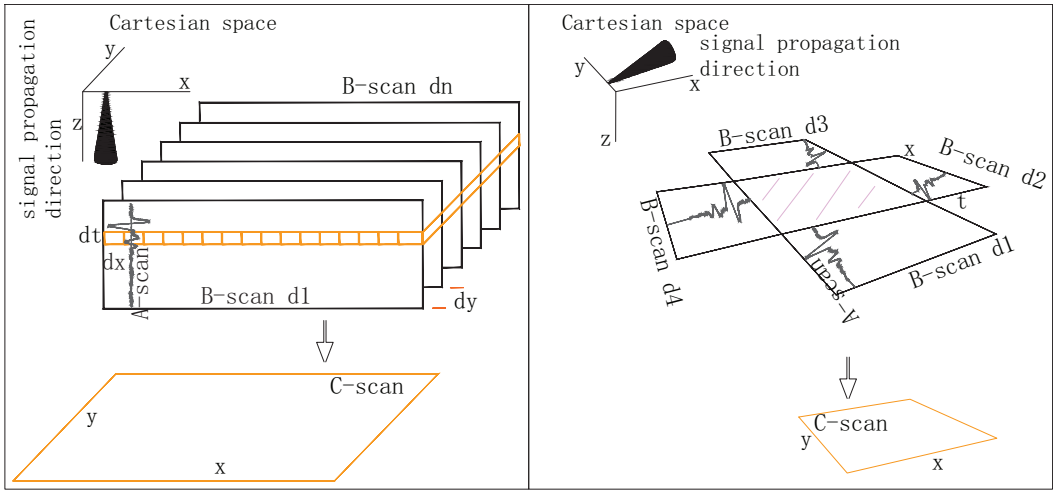


Figure 13. Representation of the construction of horizontal time slices from standard two-dimensional GPR profiles in a grid delineated by x and y values, where dy is the distance between profiles; dx is the distance along the profiles, where the reflected waves are averaged; and dt is the thickness of the slices, measured in nanoseconds (double travel time). The mean of the square of the amplitudes, in the dx, dt windows and located at x, y in the grid, is the parameter displayed in the amplitude anomaly maps.

Discontinuities in the low values (blue shades) can be detected from left to right of each. The combination performed with perimeter tomography allowed us to obtain a section on the XY plane. By appropriately tuning the color scale and the values in the color palette, we arrive at the following Figure 15. In this flat slice, four anomalies were identified, comparable in size to drilled piles with a diameter of 0.8 m. These anomalies are located at the corners of the foundation a little less than 1 m inward. In the following 3D image (Figure 16), the perimeter and horizontal tomographic section are placed in the ground and make the pile anomalies visible (circled with black dotted lines).

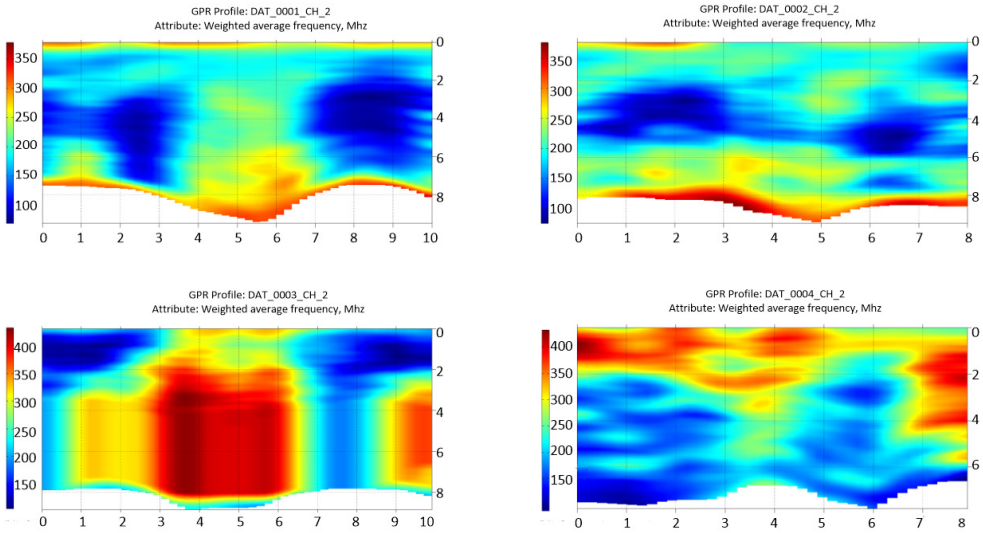


Figure 14. Result of BSEF analysis of each radargram: section of the attribute Weighted average frequency (in Mhz).

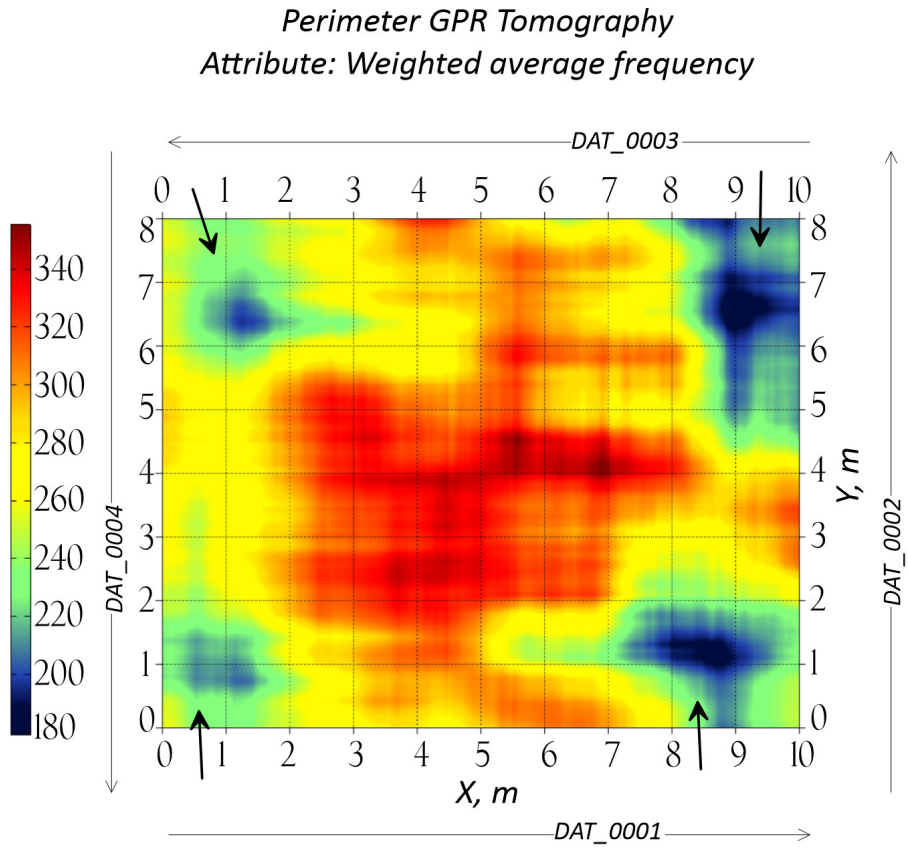


Figure 15. Result of BSEF analysis and combined section of the attribute Weighted average frequency (in Mhz); the arrows highlight the 4 anomalies.

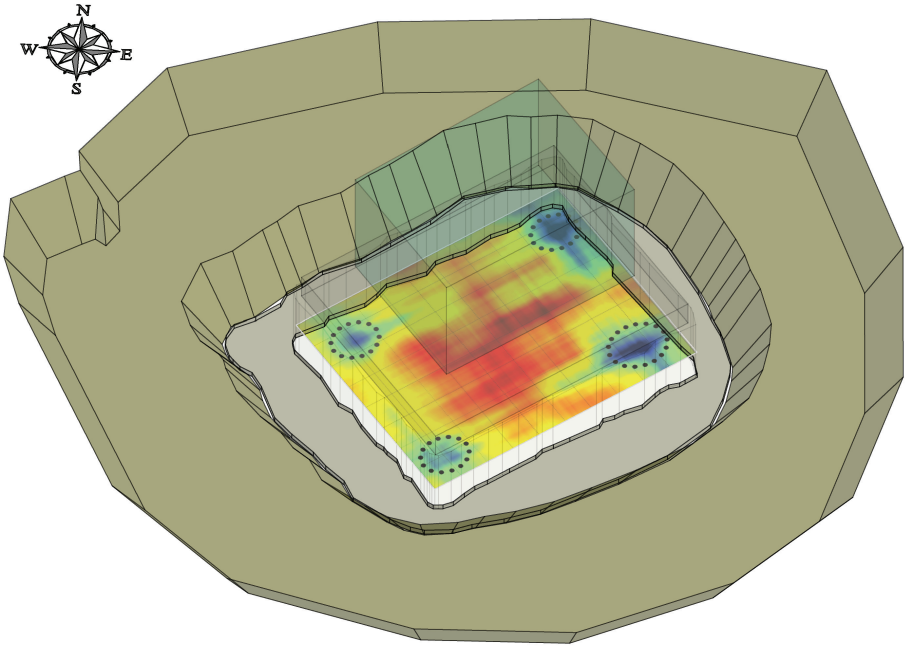


Figure 16. Overlay of the perimeter tomography to the 3D model of the structure investigated below the plinth. The anomalies of the piles have been circumscribed here. The color scale ranges from blue to red. The values with the lowest weighted average frequency are in blue, and the values whit the highest weighted average frequency are in red.

4. Discussion

We conducted a study on the search for bored piles below a large and deep foundation using GPR methods and a medium–low frequency of acquisition. Exploring a foundation plinth, and especially the piles at its base, with GPR, is difficult if approached from ground level (as explained below with the simulation). The geometry between the data acquisition plane, the position of the piles, and the aperture angle of the illumination cone is unfavorable.

The possibility of investigating the target is significantly reduced when the plinths are very thick and placed 4 m below ground level, as was addressed in this study. For an acquisition performed from ground level, the depth to be reached of several meters, as in this case, certainly falls within the potential of GPR, using low frequencies. However, the target to be investigated, the piles, would be located at a considerable distance from the GPR antennas, and both the radiation lobe and the pile are approximately parallel to each other. Furthermore, as the antenna moves toward the structure, the circular cross-section of a pile in the target area would be struck at varying angles. These increasingly smaller angles would be critical, and the returning echoes would not be picked up at the surface. To pursue a rigorous interpretation, we analyzed all aspects related to the survey and the data. The characteristics of the survey are as follows:

- The lowest operating frequency is about 134 Mhz (peak of the spectrum in Figures 11 and 12), and the wavelet pulse width is 0.27 m.
- Due to local physical properties, we know that concrete has low electrical conductivity compared to clayey silts, while velocity tests indicate acceptable dielectric permittivity contrasts because they range from 5.9 to 16.
- The soil investigated is dry and has low permeability, and no features are detected that could cause strong signal dispersion.
- The vertical resolution is about 0.14 m, and the investigation depth is about 8 m.
- The Tx-Rx separation distance is 68 cm.

Data characterizations for visual analysis include the following considerations:

- The first useful signal is measured as early as 15 ns, while the last one is measured at 175 ns.
- The attenuation of the traces is minimal (as evidenced in Figures 11 and 12 on the right); moreover, the reflections show an amplitude ranging from a minimum of −17 to a maximum of 2200.
- In the wavelet signals, one does not find polarity reversals leading to a pile interface, but one finds diffuse reversals along the entire distance axis.
- Unfortunately no hyperbolic features emerge; for direct identification of the pile, one might expect a hyperbola since it is assimilated to a cylinder.
- No point reflectors are detected.
- Linear features emerge (the wavelet offset at a certain time is zero) that might indicate a flat interface or dipping across the entire radargram. We would expect a flat interface only at the progressives where the pile is. Also, there is no obvious reflector below which other reflectors emerge.

Since the propagation and response of electromagnetic waves near the pile and near the plinth is really complex, for the correct interpretation of the radargrams, it was essential to prepare a geophysical model (Figure 17). This is to have a comparison of what might happen to signals recorded with an acquisition conducted from the surface.

In the absence of piles (left of figure), electromagnetic waves are reflected only at the interfaces of layers with different impedance. GPR traces are easily interpreted.

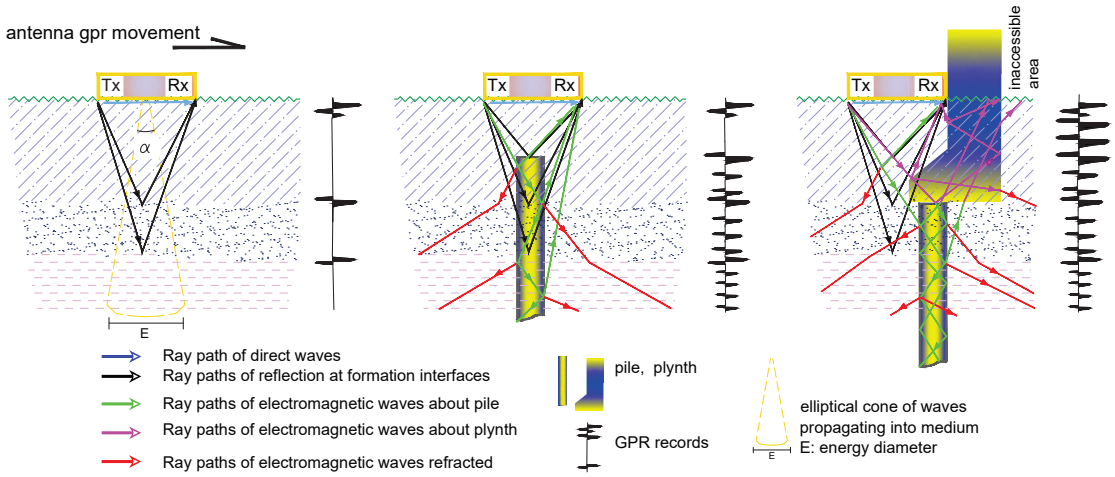


Figure 17. Geophysical modeling of electromagnetic propagation, in various layers of the subsoil (colored hatch), in the presence of foundation piles and plinths using a GPR prospection conducted from the surface.

In the presence of a pile (center of figure), reflections are always formed in the layer interfaces and in more complex reflections. They are both transmitted, refracted and guided waves in the pile and between the pile and the soil layer. Therefore, responses with relatively stable frequency and amplitude are formed in the GPR trace. Still, it is possible to distinguish reflections in the pile top.

In the presence of a plinth and the pile (right part of the figure), in addition to the formation of the waves already described for the pile, additional waves will be formed from refractions and reflections and additional guided waves in the plinth. The energy distribution of electromagnetic waves will now be changed more, which will affect the response of the GPR. In particular, the amplitude becomes weaker (response characteristics as at left) or stronger (response characteristics as at center). The frequency also becomes lower or higher, but for the oscillating waves appearing, we hypothesize that this may be due to the guided wave phenomenon generated by electromagnetic waves within or between the pile, plinth and pylon.

Instantaneous attributes, shown in Figure 18, were extracted for the acquired radargrams with the Hilbert transform: at the top the positive envelope of the traces (instantaneous amplitude) and at the bottom the instantaneous phase. In the instantaneous amplitude section, the most intense envelope traces on the positive axis (black contour) range from a minimum of 80 dB to a maximum of 118 dB, with widths from a minimum of 10 ns to a maximum of 37 ns.

In the phase section, a weak anomaly is identified at about 2 m and 25 ns and a second, but lateral, variation from 7 m to 9 m and from about 0 ns to 100 ns (white boxes). Compared with the BSEF analysis of the weighted average frequency attribute of the individual radargrams (Figure 14), here one would expect informative anomalies on both the instantaneous amplitude section, and the phase section indicating the presence of the piles. Differences in electromagnetic properties between the subsurface, the pile, and the plinth should cause changes in the GPR response. This response should manifest itself in changes in waveform, amplitude, frequency, phase, and related attributes. However, unambiguous and clearly evident variations are visible only in the frequency attribute sections, particularly in the weighted average frequency (Figure 14). To test the applicability of the method, it was necessary to conduct a simulation with scans taken from the surface to verify the response according to the geometric variables (defined in Figure 1) and the parameters of the media involved. Thus a model (Figure 19 on the left) was constructed

where on one side there was only one pile (in blue without the overlying basement) and on the other side the pile with the basement. The depth of the pile head is 4 m. The simulation led to the following result (Figure 19 on the center and right): when the values of the geometry and permittivities are identical to those of the known real case, by prospecting from the surface, reflections are obtained. In the synthetic radargram at 300 Mhz, a hyperbola (progressive 2 m) with numerous multiples is formed in the center at the single blue pile; however, the hyperbola is sharp. On the pile side with the basement (progressive 7.5 m), flat reflections are obtained in the first 100 ns with crossed multiples and numerous reverberations on the edges of the structure in the first 90 ns.

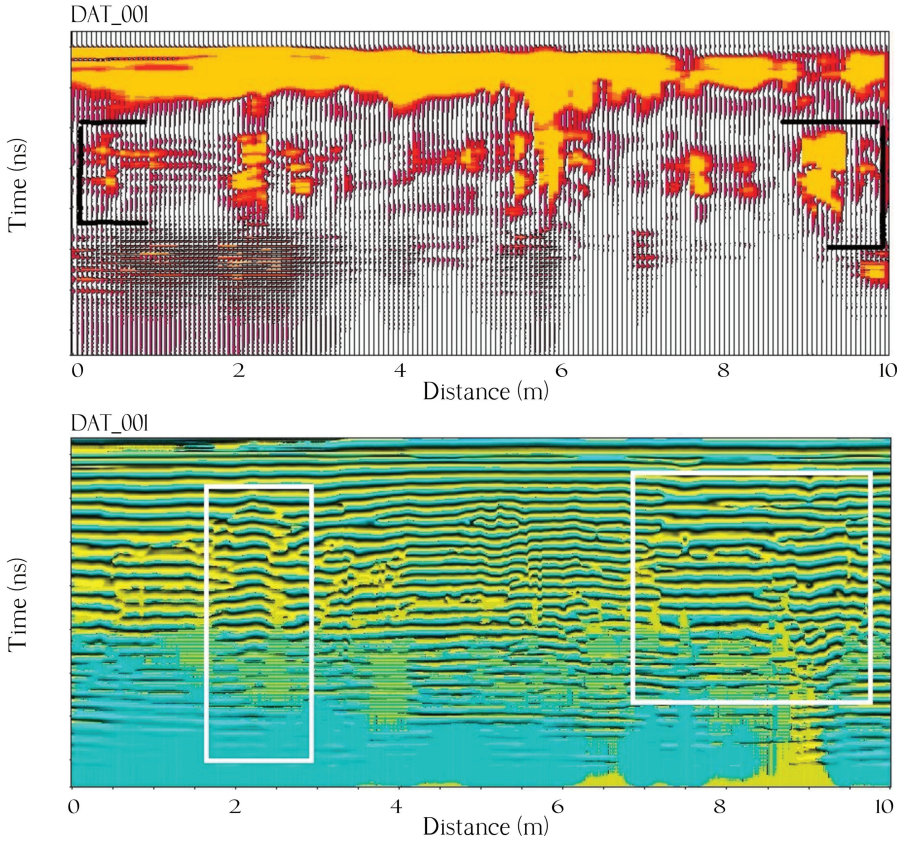


Figure 18. Attribute sections of the instantaneous amplitude and phase of the radargram DAT_001. The boxes highlight the areas of anomaly.

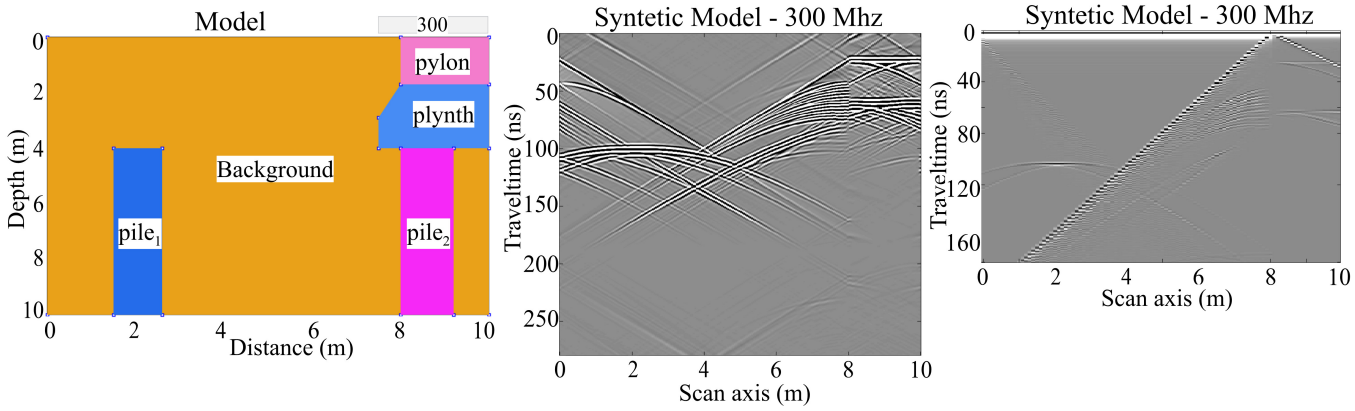


Figure 19. (**Left**) is the initial model; the colors indicate different permittivities and electrical conductivities; in the (**center**) there is the simulation with the TM-mode, Finite Difference, time-domain method [38]; on the (**right**), the simulation with doubled dielectric permittivity ratios and method Split-step 2D [39].

Changes in polarity and amplitude alone do not help to understand the onset of the pile and its development. A strong disturbing element is cross reflections related to guided waves throughout the radargram.

In the synthetic radargram at 300 Mhz, right, the dielectric permittivity ratios between the media have been doubled while leaving other geometric values unchanged. A more defined hyperbola (progressive 2 m) with a single multiple is formed at the single blue pile. On the side of the pile with the basement (progressive 7.5 m), we now obtain two plane reflections in the first 100 ns with a single multiple. On the edges of the structure, however, reverberations always emerge in the first 90 ns. Again, a strong disturbing element here is the cross reflections associated with guided waves throughout the radargram. Changes in polarity and amplitude alone could now only help to discriminate pile beginnings if the construction depths are known a priori. With the scans that were possible on the opposite faces of the excavations, the data are acquired perpendicular to the pile axis, and they do not contain guided wave noise, reverberations and multiples.

Extraction of weighted average frequency attributes and combination in perimeter tomography eliminates any interpretative ambiguity. Ultimately, scans from the surface can provide the presence of the pile even at depths of 4 m if it is without the basement. In the presence of the plinth in the GPR response signals, it can be very complex to extract pile information. The limitation of the automated BSEF analysis method is that the real part of the complex permittivity ϵ' cannot be calculated from the parameters of the diffraction component of the wave field if this component is absent on the GPR profile. The reasons for the absence of a diffraction component may be one of the following:

- Absence of local inhomogeneities whose linear dimensions are comparable to the wavelength of the GPR probing pulse.
- Large step of GPR profiling (aliasing).

In natural and artificial strata, there are always local objects of various scales and natures that are the source of diffracted waves, so even for small permittivity contrasts (e.g., when the difference of $\epsilon < 3$), this method can be used because it counts the presence of local objects that create diffracted waves.

5. Conclusions

In this study, a new approach for GPR detection of large-diameter piles below a deep, massive foundation is presented. The approach involves performing GPR tests on the exposed faces of the perimeter excavation carried out up to 6 m depth, processing the data and, in particular, with BSEF analysis and testing the results by comparing simulated synthetic radargrams with acquisitions from the surface. GPR tests in the field were conducted to evaluate the foundation problem on piles. The pile depth information provided by the GPR evaluation is useful and important in resolving the engineering dispute about the actual number of piles present at the base of the plinth.

The transillumination and CMP acquisition methods were used to estimate the wave velocity in the investigated media. Based on the EM wave velocity, the investigation depths were estimated. For good penetration of the EM signal at great depth, the antenna with low center frequency was used, which is essential to provide high-energy waves in order to detect deep objects. This study presents the application of combined and sequential use in transmission and reception of 300 and 200 Mhz antennas. Single radargrams, after post-processing and extraction of instantaneous amplitude and phase, show anomalies, which cannot be unambiguously interpreted, leaving an ambiguous solution if no a priori knowledge is available. Similarly, simulation tests generate radargrams with anomalies affected by a minimum of guided wave disturbance after doubling the ratios of dielectric permittivity values. However, correct interpretation of the data always requires a

priori knowledge of the geometries involved. Conversely, the scans performed below the plinth on which they rest produced the anomalies, but combining the sections in the form of "perimeter tomography". In fact, the scans are performed on the same plane but in different directions.

The BSEF analysis of the radargrams and the study of the weighted average frequency attribute sections allowed the detection of pile anomalies already in the single radargrams. These, in turn, combined in the form of perimeter tomography, clearly showed the presence of four piles below the plinth. The technique of backscattered field analysis made it possible to interpret the data unambiguously, leading to an accurate answer as to the number of existing engineering structures. The assumptions adopted in the analysis made the computational process much easier and more accurate, thanks to the velocity tests performed. GPR prospecting in conjunction with advanced data processing proved to be an effective and reliable technique in providing accurate information on the presence, number and location of large-diameter piles below a massive plinth. The results show a favorable accuracy that emerged with a robust analysis of the data with respect to the chosen detection geometry. Further studies will expand this work and will be aimed at investigating the variation in the minimum and maximum angle between the target and the radiation lobe of the antennas, with respect to which the presence of the piles could still be probed, moving the antennas along the vertical axis.

Funding: This research received no external funding.

Data Availability Statement: No data are associated with this research.

Acknowledgments: I thank Roman R. Denisov for his technical contribution, his computer support and advice, and his checks on data processing. I thank Paolo Spallacci for the opportunity provided to perform the georadar surveys.

Conflicts of Interest: The author declares no conflicts of interest.

Abbreviations

The following abbreviations are used in this manuscript:

BSEF	Backscattering Electromagnetic Field
CMP	Common Mid Point
EM	Electromagnetic
GPR	Ground-Penetrating Radar
RDP	Relative Dielectric Pemittivity
Rx	Receiver
SNR	Signal-to-Noise Ratio
Tx	Transmitter
UWB	Ultra-Wide Band

References

1. Paoletti, V.; D'Antonio, D.; De Natale, G.; Troise, C.; Nappi, R. Large-Depth Ground-Penetrating Radar for Investigating Active Faults: The Case of the 2017 Casamicciola Fault System, Ischia Island (Italy). *Appl. Sci.* **2024**, *14*, 6460. [CrossRef]
2. Nappi, R.; Paoletti, V.; D'Antonio, D.; Soldovieri, F.; Capozzoli, L.; Ludeno, G.; Porfido, S.; Michetti, A.M. Joint Interpretation of Geophysical Results and Geological Observations for Detecting Buried Active Faults: The Case of the "Il Lago" Plain (Pettoranello Del Molise, Italy). *Remote Sens.* **2021**, *13*, 1555. [CrossRef]
3. Alani, A.M.; Morteza, A.; Gokhan, K. Applications of Ground Penetrating Radar (GPR) in Bridge Deck Monitoring and Assessment. *J. Appl. Geophys.* **2013**, *97*, 45–54. [CrossRef]
4. Soldovieri, F.; Persico, F.; Utsi, E.; Utsi, V. The Application of Inverse Scattering Techniques with Ground Penetrating Radar to the Problem of Rebar Location in Concrete. *NDT Int.* **2006**, *39*, 602–607. [CrossRef]

5. D'Antonio, D.; Di Stefano, S.; Faustoferri, A.; De Leo, A. Opi (AQ) Ponte Romano Sul Sangro. *Quad. Archeol. D'Abruzzo* **2014**, *5*, 128–134.
6. Lai, W.L.; Kou, S.C.; Tsang, W.F. Characterization of Concrete Properties from Dielectric Properties Using Ground Penetrating Radar. *Cem. Concr. Res.* **2009**, *39*, 687–695. [CrossRef]
7. Tosti, F.; Slob, E. Determination, by Using GPR of the Volumetric Water Content in Structures, Substructures, Foundations and Soil, Civil Engineering Applications of Ground Penetrating Radar. In *Springer Transaction in Civil and Environmental Engineering*; Springer: Cham, Switzerland, 2015.
8. Morozov, P.; Morozov, F.; Lazarev, M.; Popov, A. Characterization of Antenna Radiation Pattern and Penetration Depth in Ground Penetrating Radar Field Missions. *Remote Sens.* **2023**, *15*, 5452. [CrossRef]
9. Zhou, D.; Zhu, H. Application of Ground Penetrating Radar in Detecting Deeply Embedded Reinforcing Bars in Pile Foundation. *Hindawi Adv. Civ. Eng.* **2021**, *2021*, 4813415. [CrossRef]
10. Diamanti, N.; Annan, P. Characterizing the energy distribution around GPR antennas. *J. Appl. Geophys.* **2013**, *99*, 83–90. [CrossRef]
11. Bradford, J.H. Frequency Dependent Attenuation of GPR Data as a Tool for Material Property Characterization: A Review and New Developments. In Proceedings of the 6th International Workshop on Advanced GPR, Aachen, Germany, 22–24 June 2011; pp. 1–4.
12. Grandjean, G.; Gourry, J.C.; Bitri, A. Evaluation of GPR Technique for Civil-Engineering Applications: Study on a Test Site. *Appl. Geophys.* **2000**, *45*, 141–156. [CrossRef]
13. Annan, A.P. *Ground Penetrating Radar Principles, Procedures and Applications*, Sensor and Software ed.; Sensors & Software Inc.: New York, NY, USA, 2003; Volume 278.
14. Davis, J.L.; Annan, A.P. Ground Penetrating Radar for High-Resolution Mapping of Soil and Rock Stratigraphy. *Geophysics* **1989**, *37*, 531–551.
15. Annan, A.P.; Cosway, S.W. Symposium on the Application of Geophysics to Engineering and Environmental Problems. In *Ground Penetrating Radar Survey Design*; Environmental & Engineering Geophysical Society: New York, NY, USA, 1992.
16. Daniels, D.J. *Ground Penetration Radar*, 2nd ed.; Number 15 in IEE Radar, Sonar and Navigation; Institut of Engineering & Technology: London, UK, 2004.
17. Burger, H.R. *Exploration Geophysics of the Shallow Subsurface*, Englewood Cliffs ed.; Print Hall: Hackensack, NJ, USA, 1992.
18. Conyers, L.B. *Ground-Penetrating Radar for Archaeology*; AltaMira Press: Walnut Creek, CA, USA, 2004.
19. Skolnik, M.I. *Introduction to Radar System*, 3rd ed.; MacGraw-Hill: New York, NY, USA, 2001; Volume 278, pp. 3–5.
20. Wu, Y.; Shen, F.; Liu, R. An ultra-wideband antenna with low dispersion for ground penetrating radar system. *IEEE Sens. J.* **2021**, *21*, 15171–17179. [CrossRef]
21. Lavoue, F. 2D Full Waveform Inversion of Ground Penetrating Radar Data: Towards Multiparameter Imaging from Surface Data. Ph.D. Thesis, Université de Grenoble, Sigillum Universitatis Gratianopolitane, Saint-Martin-d'Hères, France, 2014.
22. Klysz, G.; Balayssac, J.P. Determination of Volumetric Water Content of Concrete Using Ground-Penetrating Radar. *Cem. Concr. Res.* **2007**, *37*, 1164–1171. [CrossRef]
23. Moysey, S.; Knight, R.J. Modeling the field-scale relationship between dielectric constant and water content in heterogeneous systems. *Water Resour. Res.* **2004**, *40*, W03510. [CrossRef]
24. Jonscher, A.K. Dielectric relaxation in solids. *J. Phys. D Appl. Phys.* **1999**, *32*, 57–70. [CrossRef]
25. Olhoeft, G.R. Maximizing the Information Return from Ground Penetrating Radar. *J. Appl. Geophys.* **2000**, *43*, 175–187. [CrossRef]
26. Zhao, W.; Forte, E.; Pipan, M. Texture attribute analysis of GPR data for archaeological prospection. *Pure Appl. Geophys.* **2016**, *173*, 2737–2751. [CrossRef]
27. Khwanmuang, W.; Udphuay, S. Ground-penetrating radar attribute analysis for visualization of subsurface archaeological structures. *Lead Edge* **2011**, *31*, 946–949. [CrossRef]
28. Tronicke, J.; Böniger, U. GPR attribute analysis: There is more than amplitudes. *First Break* **2013**, *31*, 103–108. [CrossRef]
29. Giannopoulos, A. GprMax2D V 1.5 User's Manual. 2002. Available online: https://www.gprmax.com/ (accessed on 10 October 2024)
30. Persico, R. *Introduction to Ground Penetrating Radar: Inverse Scattering and Data Processing*; Wiley-IEEE Press: Hoboken, NJ, USA, 2014.
31. Radzevicius, S.; Daniels, J.J. Ground Penetrating Radar Polarization and Scattering from Cylinders. *J. Appl. Geophys.* **2000**, *45*, 111–125. [CrossRef]
32. Langley, K.A.; Hamrain, S.E. Use of C-band Ground Penetrating Radar to Determine Backscatter Sources within Glaciers. *IEEE Trans. Geosci. Remote Sens.* **2005**, *45*, 1236–1246. [CrossRef]
33. Denisov, R.R. Processing of georadary data in automatic mode. *Sci. Tech. J. Geophys.* **2010**, *4*, 76–80.
34. Ulaby, F.T.; Moore, R.K.; Fung, A.K. Microwave Remote Sensing Active And Passive Volume Ii Radar Remote Sensing and Surface Scattering and Emission Theory. In *Radar Remote Sensing and Surface Scattering And Emission Theory*; Addison-Wesley Publishing Company: Boston, MA, USA, 1982; Volume II.

35. Toropainen, A.P. Measurement of the Properties of Granular Materials by Microwave Backscattering. *J. Microw. Power Electromagn. Energy* **1995**, *30*, 240–245. [CrossRef]
36. González, R.C.; Woods, E.C.; Eddins, S.L. *Digital Image Processing Using MATLAB*; Pearson Prentice Hall: Saddle River, NJ, USA, 2003.
37. Ivan Levyant, V.B.; Petrov Pankratov, S.A. Seismic Exploration Technologies. In *Research of the Characteristics of Longitudinal and Exchange Waves of Retroactive Response Scattering from the Zones of the Cracked Collector*; Moscow Institute of Physics and Technology: Moscow, Russia, 2009; pp. 3–11.
38. Irving, J.; Knight, R. Numerical modeling of ground-penetrating radar in 2-D using MATLAB. *Comput. Geosci.* **2006**, *32*, 1247–1258. [CrossRef]
39. Bitri, A.; Grandjean, G. Frequency–wavenumber modelling and migration of 2D GPR data in moderately heterogeneous dispersive media. *Geophys. Prospect.* **1998**, *46*, 287–301. [CrossRef]

Disclaimer/Publisher's Note: The statements, opinions and data contained in all publications are solely those of the individual author(s) and contributor(s) and not of MDPI and/or the editor(s). MDPI and/or the editor(s) disclaim responsibility for any injury to people or property resulting from any ideas, methods, instructions or products referred to in the content.